

Simultaneous mapping of nanoscale dielectric, electrochemical, and ferroelectric surface properties of van der Waals layered ferroelectric via advanced SPM

Cite as: Appl. Phys. Lett. **119**, 252905 (2021); <https://doi.org/10.1063/5.0078034>

Submitted: 09 November 2021 • Accepted: 04 December 2021 • Published Online: 21 December 2021

 M. Checa,  S. M. Neumayer, M. A. Susner, et al.

COLLECTIONS

 This paper was selected as Featured



[View Online](#)



[Export Citation](#)



[CrossMark](#)

ARTICLES YOU MAY BE INTERESTED IN

Emerging van der Waals ferroelectrics: Unique properties and novel devices
Applied Physics Reviews **8**, 021316 (2021); <https://doi.org/10.1063/5.0028079>

Spiral high-speed scanning tunneling microscopy: Tracking atomic diffusion on the millisecond timescale

Applied Physics Letters **119**, 251601 (2021); <https://doi.org/10.1063/5.0071340>

Ferroelectric or non-ferroelectric: Why so many materials exhibit “ferroelectricity” on the nanoscale

Applied Physics Reviews **4**, 021302 (2017); <https://doi.org/10.1063/1.4979015>

Lock-in Amplifiers
up to 600 MHz



Zurich
Instruments



Simultaneous mapping of nanoscale dielectric, electrochemical, and ferroelectric surface properties of van der Waals layered ferroelectric via advanced SPM

Cite as: Appl. Phys. Lett. **119**, 252905 (2021); doi: [10.1063/5.0078034](https://doi.org/10.1063/5.0078034)

Submitted: 9 November 2021 · Accepted: 4 December 2021 ·

Published Online: 21 December 2021



View Online



Export Citation



CrossMark

M. Checa,^{1,a)}  S. M. Neumayer,¹  M. A. Susner,² M. A. McGuire,³  P. Maksymovych,¹ and L. Collins^{1,a)} 

AFFILIATIONS

¹Center for Nanophase Materials Sciences, Oak Ridge National Laboratory, Oak Ridge, Tennessee 37831, USA

²Materials and Manufacturing Directorate, Air Force Research Laboratory, Wright-Patterson Air Force Base, Dayton, Ohio 45433, USA

³Materials Science and Technology Division, Oak Ridge National Laboratory, Oak Ridge, Tennessee 37831, USA

^{a)}Authors to whom correspondence should be addressed: checam@ornl.gov and collinslf@ornl.gov

ABSTRACT

Ferroelectric surfaces involve a complex interplay between polarization and dielectric properties, internal and external surface charge screening, and ionic and electrochemical effects. There is currently no good way to simultaneously capture all the required information at appropriate length scales. To this end, we present an advanced scanning probe microscopy approach for simultaneously mapping surface potential, dielectric, and piezoelectric properties on the nanoscale. For quantitatively mapping electromechanical properties, we utilize interferometric displacement sensing piezoresponse force microscopy, which measures the effective piezoelectric coefficient free of background artifacts such as the cantilever body electrostatics. The dielectric and surface electrochemical properties are captured during G-mode electrostatic force microscopy/Kelvin probe force microscopy operated in the lift mode. We show the capabilities of this approach on the chemically phase separated composite sample consisting of a van der Waals layered ferroelectric CuInP₂S₆ phase and a non-polar In_{4/3}P₂S₆ phase. Finally, we demonstrate domain structure evolution during thermally stimulated phase transition.

Published under an exclusive license by AIP Publishing. <https://doi.org/10.1063/5.0078034>

Ferroelectricity underpins a broad range of applications from ferroelectric sensors and actuators¹ to random-access memories² or tunnel junctions.³ However, even after decades of research, the physical and chemical properties of ferroelectric surfaces and interfaces are often poorly understood.⁴ This is largely due to the fact that the spontaneous polarization can initiate a complex interplay between several physical and chemical properties, which can be seen in a variety of phenomena such as internal and external screening,⁵ band bending,⁶ bulk or surface electrochemical and ionic effects,⁷ as well as tunable dielectric response.⁸ A better understanding of ferroelectric materials necessitates new approaches to microscopy and correlative imaging, which can simultaneously probe a range of complementary properties.

Piezoresponse force microscopy (PFM) is arguably the most popular approach for nondestructive probing of local piezoelectric properties and/or visualization of ferroelectric nanodomains via the detection of electromechanical responses at surfaces. Relentless development of PFM imaging and spectroscopic methods enabled measurements of

important physical characteristics such as piezoelectric coefficients,⁹ nucleation bias/coercive fields,¹⁰ energy dissipation,¹¹ and domain wall dynamics.¹² PFM has also been extended to allow probing of more exotic phenomena including dielectric tunability,⁸ flexoelectricity,¹³ and even ionically mediated Vegard strains in non-ferroelectric materials (e.g., electrochemical strain microscopy¹⁴).

However, PFM and related methods are known to suffer from intrinsic artifacts, which are thought to have contributed to a rise in reports of ferroelectricity in materials, which are known not to be ferroelectric.^{15,16} In particular, PFM is complicated by signal contributions that arise from background electrostatics interactions between the cantilever body and the sample.^{17,18} These electrostatic artifacts are often difficult to distinguish from cantilever vibrations originating from real piezoelectric response. Therefore, artifact-free PFM methods are needed for quantification of the true tip displacement, a necessity for reliable quantification of complex domain structures, nanoscale size-effects, and dynamic information. One such method is interferometric displacement

sensing piezoresponse force microscopy (IDS-PFM),^{19–22} which has been shown to be largely free from electrostatic influences when the detection laser is positioned over the tip location, and unlike optical beam approaches, which detects cantilever bending (or slope), IDS-PFM provides a direct displacement measurement. Even still, uncertainties often exist surrounding the surface and tip condition, electric field distribution under the tip, possible substrate clamping, and higher order electromechanical effects all of which complicate absolute quantification of the true underlying electromechanical phenomena. These last factors can be particularly important in ultrathin films or 2D materials, required for miniaturization of ferroelectric devices. Hence, it is important to explore complementary methods, which can be used in conjunction with PFM to reveal insight into other functional properties of the ferroelectric surface.

For studying dielectric and electrochemical properties, non-contact modes of operation, such as Kelvin probe force microscopy (KPFM) and electrostatic force microscopy (EFM), can be utilized.⁵ KPFM is the gold standard technique of choice to map the local surface potential²³ and has been extensively used to map ferroelectric domains^{24,25} and understand polarization screening²⁶ and charge injection²⁷ in ferroelectric surfaces. Meanwhile, EFM was used to image a domain pattern²⁸ and to study the effects of environmental conditions²⁹ but generally not as widely used compared to other techniques. In particular, whereas EFM has been extensively used for dielectric characterization inferred from the second harmonic response signal [see Eq. (2)] in a variety of different systems like nanoparticles,³⁰ 2D materials,^{31,32} buried nanostructures,³³ devices,³⁴ or biological samples,^{35–37} the characterization of ferroelectrics has been limited due to the loss of sensitivity of the technique for high dielectric constant samples³⁸ (which is the case for most ferroelectrics). In addition, the procedure to achieve quantification is rather complex. Therefore, other impedance-based approaches, like scanning microwave microscopy (SMM)^{39,40} or scanning non-linear dielectric microscopy (SNDM),^{41,42} are more widely applied to ferroelectrics, although their quantification is also quite challenging.

Here, we combine quantitative IDS-PFM with G-mode electrostatic force microscopy/Kelvin probe force microscopy (G-mode EFM/KPFM). This approach allows simultaneous mapping of electromechanical, electrochemical, and dielectric properties, which we demonstrate on a chemically phase separated composite sample consisting of a van der Waals (vdW) layered ferroelectric CuInP₂S₆ (CIPS) phase and a non-polar In_{4/3}P₂S₆ (IPS) phase.⁴³ We reveal a local dielectric contrast between the different chemical phases of the material, linked to ferroelectricity, as well as different ionic conductivity and dielectric loss between CIPS and IPS. Most notably, the dielectric contrast allows one to monitor the different chemical domains even in conditions where PFM fails (such as when the material is in its paraelectric state). We envision this technique will be most impactful in applications in nanoscale and 2D ferroelectrics, proximity of phase transitions and disordered materials, where either phase competition or size effects dramatically suppress polarization and piezoelectric response.

In Fig. 1, we present a scheme of the two-pass mode experimental setup used for the measurements. Two-pass mode means that the tip performs two consecutive scans line by line. During the first pass, the tip scans the surface in the contact mode, while an electrical AC excitation of amplitude V_{PBM} and frequency ω_{PBM} is applied to it, thus generating a periodic deformation in the material that is captured by

means of IDS-PFM.^{19,20} The IDS-PFM signal is demodulated by a lock-in amplifier that directly generates the subsequent amplitude and phase images, free of electrostatic artifacts, which can be converted to the out of plane effective piezoelectric coefficient d_{eff} just by dividing the measured amplitude signal by the applied voltage V_{PBM} .

During the second pass, the tip is lifted to a certain height and scans the surface out-of-contact, while a different electrical AC excitation of amplitude V_{EFM} and frequency ω_{EFM} is applied to it, generating the well-known multi-harmonic response of EFM.⁴⁴ We employ G-mode detection, where high speed data acquisition of the real-time photodetector deflection signal is utilized in optical beam detection (OBD). This signal will be properly postprocessed later to obtain the different harmonic contributions (see mode details about the postprocessing steps in [supplementary material S1](#) and elsewhere⁴⁵). One advantage of using the digital processing approach vs the standard lock-in amplifier detection is the accessibility to the raw data, which we can explore through filtering approaches based on signal processing or machine learning (see [supplementary material S2](#) for the application of principal component analysis decomposition of the G-mode EFM/KPFM data) as well as allowing a prior knowledge of the noise system.

Once the different harmonic components are retrieved from the cantilever movement data stream, one can use the well-known relationships between the harmonics and the physical magnitudes of interest to retrieve the capacitance gradient (C'_z) and contact potential difference (V_{CPD}) images

$$F_\omega = C'_z (V_{DC} - V_{CPD}) V_{AC} \sin(\omega_{EFM} t), \quad (1)$$

$$F_{2\omega} = -\frac{C'_z}{4} V_{AC}^2 \cos(2\omega_{EFM} t), \quad (2)$$

$$V_{CPD} = \frac{V_{EFM}}{4} \frac{A_{\omega_{EFM}} \cos(\varphi_{\omega_{EFM}}) G_{2\omega_{EFM}}}{A_{2\omega_{EFM}} G_{\omega_{EFM}}}, \quad (3)$$

where A_ω and $A_{2\omega}$ are the amplitudes of the first and second harmonic oscillations, respectively, φ_ω is the phase of the first harmonic, and G_ω and $G_{2\omega}$ are the values of the cantilever transfer function at ω and 2ω , respectively. Therefore, C'_z can be obtained directly from the second harmonic response, and V_{CPD} can be obtained by means of Eq. (3). Finally, since EFM/KPFM signal generation is controlled by long range electrostatic forces, its resolution will differ from PFM and can be expected to have more contributions from the probe cone and cantilever, as explained with detail elsewhere.⁴⁶

Next, we use simultaneous characterization of electromechanical and dielectric properties to map the properties of vdW layered CIPS, which has recently gained lot of attention both in terms of fundamental properties involving multi functionality in electric, ionic, and thermal phenomena^{47,48} but also from an application point of view in capacitors,⁴⁹ field-effect transistors,^{50,51} or pyroelectric generators.⁴⁹ CIPS exhibits room temperature ferroelectricity, which arises from the different stable positions of the Cu cation within its polar crystallographic structure. Moreover, a tunable quadruple potential well leads to four different polarization states that manifest as ferroelectric domains in the material.⁵² In addition, by tuning the overall macroscopic stoichiometric composition, the non-ferroelectric Cu-free IPS phase can form, increasing the material complexity and tunability.

In Fig. 2, we show the performance of the technique. Figure 2(a) shows the topography of a 90 nm thick CIPS-IPS transferred directly

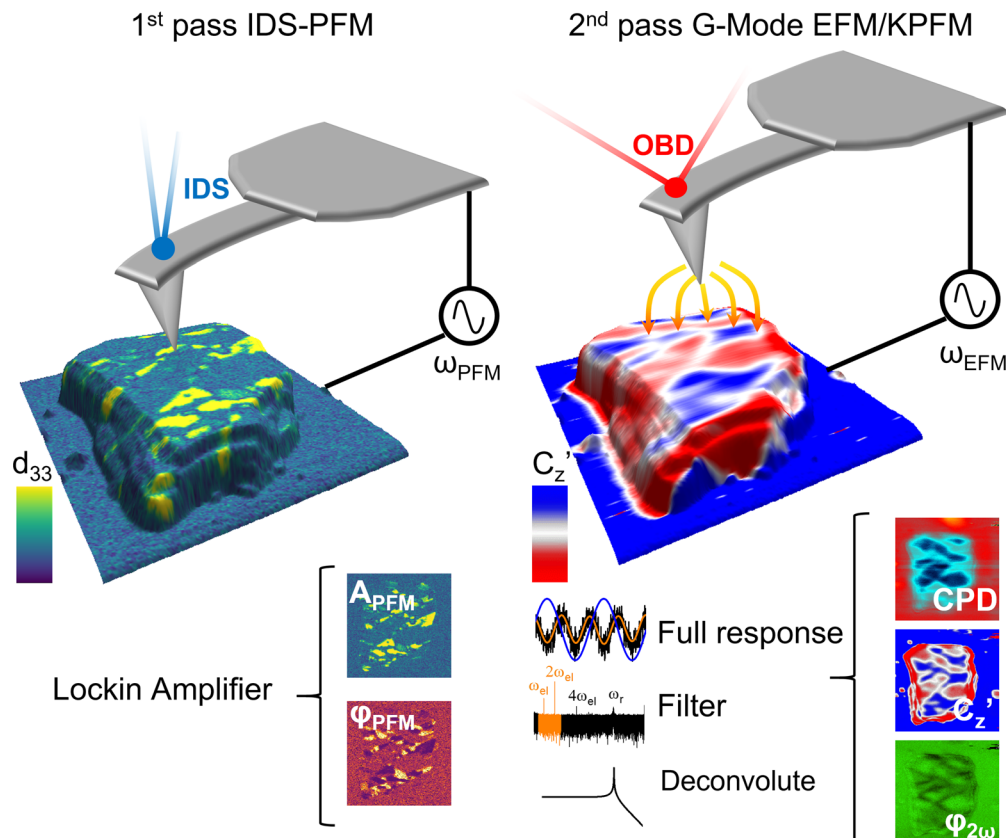


FIG. 1. Schematic of the experimental setup. First pass uses IDS-PFM in the contact mode to map piezoelectric domains (left). Second pass uses G-mode EFM/KPFM out-of-contact to map dielectric properties and the surface potential simultaneously.

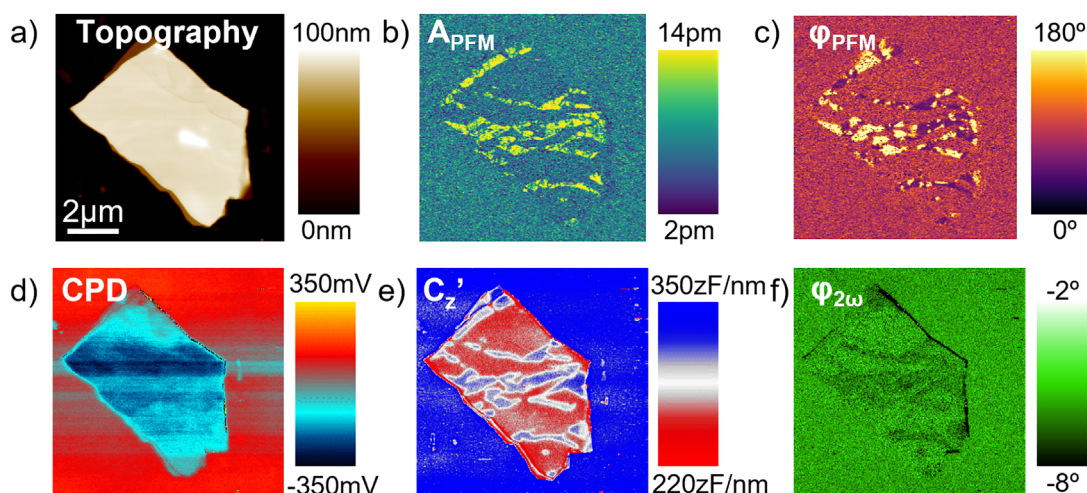


FIG. 2. Simultaneous piezoelectric, contact potential, and dielectric imaging of a 70 nm thick CIPS-IPS flake transferred onto gold. (a) Topography. (b) IDS-PFM amplitude. (c) IDS-PFM phase. (d) Contact potential difference. (e) G-mode 2ω -amplitude (capacitance gradient) and (f) G-mode 2ω -phase (resistivity).

onto a gold substrate with the scotch tape transfer method⁵³ at room temperature. Figures 2(b) and 2(c) display the IDS-PFM amplitude and phase, respectively, and denote a clear contrast between the different parts of the sample. Zones with a high PFM amplitude response correspond to ferroelectric CIPS, and the PFM phase channel identifies the domains with opposite polarization. Note that oppositely to typical observations in standard OBD-PFM where electrostatic response can provide false PFM contrast, in this case both the gold substrate and the IPS phase of the flake show the same amplitude and phase values due to their null electromechanical response, which validates the artifact-free IDS approach. In supplementary material S3, the histogram analysis of the PFM amplitude image of a thicker flake (see Fig. 3), analyzed using a masking procedure explained elsewhere,⁵² obtains a $d_{eff} = 11 \pm 4 \text{ pm/V}$, which is slightly smaller (but still is in good agreement) than the values reported for this material in bulk crystal using band excitation piezoresponse force microscopy (BE-PFM) ($\sim 16 \text{ pm/V}$).⁵² The discrepancy may be either due to differences in the flake thickness [e.g., for the 90 nm flake from Fig. 2(b)], we measure a different $d_{eff} = 8 \pm 2 \text{ pm/V}$ in agreement with previous works showing that the d_{eff} diminishes with decreasing flake thickness⁵⁴] or the fact that the BE-PFM includes contributions from electrostatics, which can be easily of a few pm/V.

In the second row, the images obtained with G-mode EFM/KPFM are shown. Figure 2(d) is the contact potential difference (CPD) image, where it is easy to distinguish between the flake and the gold substrate. Some contrast within the flake can also be seen; however, differentiating between CIPS/IPS phases is not straightforward. CPD includes useful information on charge screening and surface electrochemistry among others, and in addition in the absence of IDS-PFM, the CPD is needed to deconvolute the electrostatic component of the OBD-PFM data, being crucial for quantification of d_{eff} in standard PFM.¹⁸

Figures 2(e) and 2(f) show the G-mode 2ω -amplitude and 2ω -phase images, respectively. The 2ω -amplitude is directly linked to the capacitance gradient (C'_z) of the system [through Eq. (2)], which is dependent on both the tip and sample geometry as well as the sample's dielectric constant. Hence, considering that the flake is very flat (surface roughness is $\sim 2 \text{ nm}$ and unit cell is 1.3 nm) and their minute topographical changes are not correlated with the chemical domains (see the deflection image in supplementary material S4a, where minute steps on the flake surface are highlighted), C'_z offers a qualitative image of the dielectric constant of the sample, complementing the information obtained by PFM. The one-to-one correlation between the contrast in the PFM amplitude and C'_z indicates that the dielectric constant of the CIPS phase is higher than the IPS phase. Quantifying such measurements to achieve realistic values of the dielectric constant of the different phases present necessitates calibration of the system and to consider several additional geometric parameters, which adds complexity to the analysis and is outside of the scope of this work.⁵⁵

Finally, the 2ω -phase contrast arises from a phase shift between the AC excitation applied during the G-mode EFM/KPFM pass and the measured tip oscillation. Such a phase shift arises from local resistive phenomena happening under the tip that are triggered by the applied electric field. In our images, we observe a phase shift in the Cu containing phase, which we attribute to ionic motion triggered by the tip electrical excitation. We can safely assume this effect is not found in the Cu-free IPS phase, because there is no Cu present in such a

phase, and the fact that it is also present above T_c (see Fig. 3) confirms that is not an effect driven by polarization or screening dynamics. Therefore, this channel provides a non-contact measurement of the local dielectric losses complementing other techniques based on imaging current like conductive AFM.⁵⁶ In addition, G-mode EFM/KPFM is a gentler technique suitable also for delicate samples, and no conductive path is required. Finally, such contrast clearly present in the flake should not be confused with the abrupt phase contrast found on the right edge of the flake, which indicates that the tip likely touched the sample at that point during the second (lift) pass, as this contrast is also seen in the non-contact deflection image (S4b) and only observed in one of the edges of the flake.

Consecutively, we explore the influence of temperatures in the CIPS-IPS sample, focusing on the PFM and dielectric signals. The temperature induced ferroelectric-to-paraelectric phase transition of CIPS has its Curie temperature (T_c) around 60°C – 70°C , which is in the range of accessible temperatures for most SPM setups. Such transition is the perfect candidate to show the power of the technique we are presenting. On the one hand, the piezoelectric response that CIPS exhibits below T_c should vanish above T_c . On the other hand, according to dielectric bulk measurements,⁵⁷ the dielectric response should peak right at T_c . Thus, we decided to apply the technique at three different temperatures (30°C , 60°C , and 90°C) along the transition (Fig. 3) to monitor the changes experienced as the temperature increases.

A new 170 nm thick flake (see supplementary material S5 for the topography channel) is imaged at three different temperatures. Figures 3(a) and 3(b) show the IDS-PFM amplitude and phase images, respectively. While at 30°C , the domain pattern appears like the one in Fig. 2, at 60°C , the PFM contrast vanishes, and the different phases are no longer visible. Interestingly, at elevated temperatures (90°C), a weak PFM contrast is recovered in the CIPS regions, which may arise from Vegard strain⁵⁸ due to an increase in the copper mobility at higher temperatures.⁵⁹ Further work with IDS detection might be able to unravel the activation energies of such ionic motion free of electrostatic artifacts if a deeper study is performed, which is outside of the scope of this work.

Figure 3(c) shows the CPD contrast, which can arise from different surface charges of the corresponding domains and can be of special interest to track surface electrochemistry and study surface adsorbates. We wish to emphasize that while piezoelectric and dielectric channels are very reproducible among different flakes measured to carry out this work, the CPD channel (which is more sensitive to surface chemistry, skin layers, environmental conditions, etc.) presents slightly different qualitative behavior from sample to sample, thus probably not being the best channel to track the different phases and/or domains.

Figure 3(d) shows the G-mode C'_z images. In this case, the dielectric contrast persists along the different temperatures measured, offering a chemically sensitive channel that can be used to monitor the domains through the phase transition (where PFM fails as piezoresponse signal disappears). Quantitative comparison of C'_z images at different temperatures is limited, because they are highly affected by tip geometry (radius and angle), which may experience changes due to tip wearing, especially when PFM images are acquired simultaneously. We consider the dielectric quantification outside of the scope of this work, but we expect it should peak around T_c (as in bulk measurements⁶⁰). We want to remark that for dielectric quantification purposes, ideally the tip and sample geometry should remain unchanged,

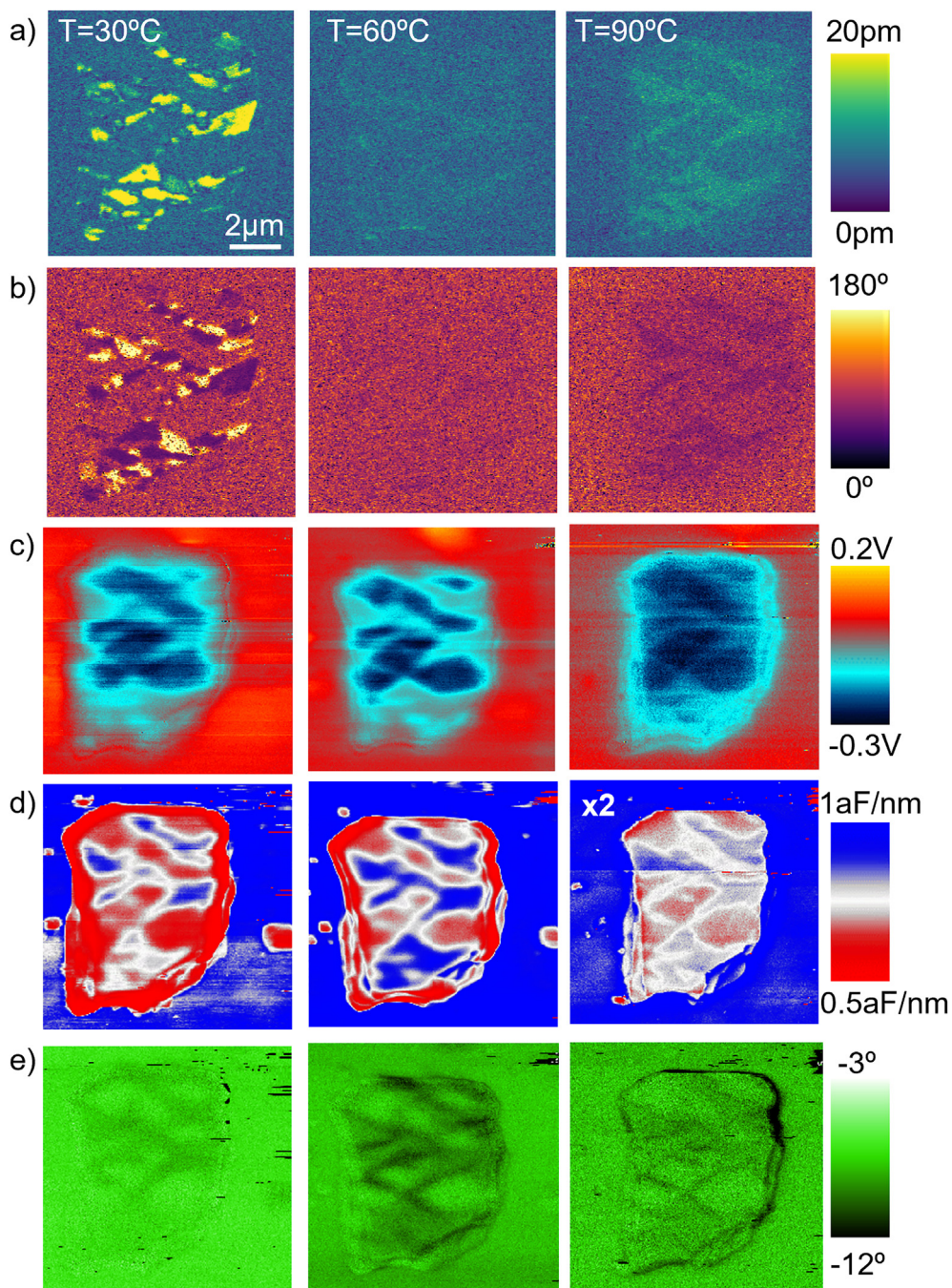


FIG. 3. Simultaneous piezoelectric, CPD, and dielectric imaging of a CIPS-IPS flake transferred onto a gold electrode at different temperatures through the ferroelectric to paraelectric phase transition. (a) IDS-PFM amplitude. (b) IDS-PFM phase. (c) CPD. (d) C_z' and (e) 2ω -phase. C_z' image at 90°C has been multiplied by a factor 2 in order to be displayed using the same colorscale.

and the tip stability should be tracked during the experiment. (This can be achieved by measuring C_z' force distance curves in the bare substrate at each step of the experiment.) In general, contact mode images (necessary for PFM) are not always the best choice as they can be a

source of tip wearing. This is clearly seen in the C_z' image at 90°C , where the image has to be multiplied by a factor 2 to be comparable with the images acquired at other temperatures using the same color scale, as probably tip changes have induced a big change in the tip

radius and angle (see [supplementary material S6](#)). In addition, especially relevant for high temperature measurements, evaporation of adsorbates/water layers that may be present could be an additional source of contrast change.

Finally, [Fig. 3\(e\)](#) shows the evolution of the G-mode 2ω -phase images with temperature, where a clear contrast is seen between the CIPS and IPS domains, indicating that we can probe the different ionic conductivity/dielectric loss of the two phases even out of contact. Especially remarkable is the fact that at 60°C , the contrast seems to be increased at the CIPS-IPS phase boundaries, which would indicate that during transition, the ionic conductivity/dielectric loss is enhanced there.

To summarize, we have demonstrated an approach to map simultaneously piezoelectricity, surface potential, and dielectric properties at the nanoscale on CIPS-IPS thin flakes. We have been able to show qualitative local dielectric contrast between the material phases, which can be of interest both to characterize such dielectric changes enabling nanoscale dielectric tunability and to track ferroelectric chemical phases even in their paraelectric state when the piezoelectricity disappears, as shown in [Fig. 3](#). In the future, we envision this approach to be useful to the ferroelectrics community, especially when expanded to provide quantitative information also from the dielectric constant side. In particular, phase transitions can be tracked reliably: as soon as PFM signals disappear due to the loss of polarization, the dielectric signal increases and still provides contrast between different chemical and structural phases.

See the [supplementary material](#) for details on G-mode signal analysis (S1), PCA analysis (S2), histogram analysis of the PFM response (S3), deflection images (S4), topography of Fig. 3 (S5), capacitance gradient force distance curves from Fig. 3 (S6), and materials and methods (S7).

This research was conducted at the Center for Nanophase Materials Sciences, which is sponsored at Oak Ridge National Laboratory by the Scientific User Facilities Division. This manuscript has been authored by UT-Battelle, LLC under Contract No. DE-AC05-00OR22725 with the U.S. Department of Energy. The United States Government retains and the publisher, by accepting the article for publication, acknowledges that the United States Government retains a non-exclusive, paid-up, irrevocable, world-wide license to publish or reproduce the published form of this manuscript, or allow others to do so, for United States Government purposes. The Department of Energy will provide public access to these results of federally sponsored research in accordance with the DOE Public Access Plan (<http://energy.gov/downloads/doe-public-access-plan>). M.A.M. acknowledges support for sample synthesis and characterization from the U.S. DOE, Office of Science, Basic Energy Sciences, Materials Sciences and Engineering Division. Authors would like to acknowledge Dr. Stephen Jesse for his assistance in developing the G-mode.

AUTHOR DECLARATIONS

Conflict of Interest

The authors have no conflicts to disclose.

DATA AVAILABILITY

The data that support the findings of this study are available from the corresponding authors upon reasonable request.

REFERENCES

- ¹P. Muralt, *J. Micromech. Microeng.* **10**(2), 136 (2000).
- ²J. Müller, T. Böscke, S. Müller, E. Yurchuk, P. Polakowski, J. Paul, D. Martin, T. Schenk, K. Khullar, and A. Kersch, in *Ferroelectric Hafnium Oxide: A CMOS-Compatible and Highly Scalable Approach to Future Ferroelectric Memories, 2013 IEEE International Electron Devices Meeting* (IEEE, 2013), pp. 10.8. 1–10.8. 4.
- ³A. Chanthbouala, A. Crassous, V. Garcia, K. Bouzehouane, S. Fusil, X. Moya, J. Allibe, B. Dlbak, J. Grollier, and S. Xavier, *Nat. Nanotechnol.* **7**(2), 101–104 (2012).
- ⁴S. M. Yang, A. N. Morozovska, R. Kumar, E. A. Eliseev, Y. Cao, L. Mazet, N. Balke, S. Jesse, R. K. Vasudevan, and C. Dubourdieu, *Nat. Phys.* **13**(8), 812–818 (2017).
- ⁵S. V. Kalinin and D. A. Bonnell, *Phys. Rev. B* **63**(12), 125411 (2001).
- ⁶B. Huang, Y. Chen, Y.-P. Chiu, Y. Huang, J. Yang, Y. Chen, and Y. Chu, *Appl. Phys. Lett.* **100**(12), 122903 (2012).
- ⁷S. V. Kalinin, S. Jesse, A. Tselev, A. P. Baddorf, and N. Balke, *ACS Nano* **5**(7), 5683–5691 (2011).
- ⁸A. Tselev, A. Klein, J. Gassmann, S. Jesse, Q. Li, S. V. Kalinin, and N. Balke, *Adv. Mater. Interfaces* **2**(15), 1500088 (2015).
- ⁹K. Kelley, D. Yilmaz, L. Collins, Y. Sharma, H. Lee, D. Akbarian, A. Van Duin, P. Ganesh, and R. Vasudevan, *Phys. Rev. Mater.* **4**(2), 024407 (2020).
- ¹⁰S. Jesse, B. J. Rodriguez, S. Choudhury, A. P. Baddorf, I. Vrejoiu, D. Hesse, M. Alexe, E. A. Eliseev, A. N. Morozovska, and J. Zhang, *Nat. Mater.* **7**(3), 209–215 (2008).
- ¹¹S. Jesse, S. V. Kalinin, R. Proksch, A. Baddorf, and B. Rodriguez, *Nanotechnology* **18**(43), 435503 (2007).
- ¹²I. Spasovic, A. Verdaguer, G. Catalan, and N. Domingo, *Adv. Electron. Mater.* **21**00650 (2021).
- ¹³A. Abdollahi, N. Domingo, I. Arias, and G. Catalan, *Nat. Commun.* **10**(1), 1266 (2019).
- ¹⁴N. Balke, S. Jesse, A. N. Morozovska, E. Eliseev, D. W. Chung, Y. Kim, L. Adamczyk, R. E. Garcia, N. Dudney, and S. V. Kalinin, *Nat. Nanotechnol.* **5**(10), 749–754 (2010).
- ¹⁵R. K. Vasudevan, N. Balke, P. Maksymovich, S. Jesse, and S. V. Kalinin, *Appl. Phys. Rev.* **4**(2), 021302 (2017).
- ¹⁶N. Balke, P. M. S. Jesse, A. Herklotz, A. Tselev, C.-B. Eom, I. I. Kravchenko, P. Yu, and S. V. Kalinin, *ACS Nano* **9**(6), 6484–6492 (2015).
- ¹⁷N. Balke, S. Jesse, B. Carmichael, M. B. Okatan, I. I. Kravchenko, S. V. Kalinin, and A. Tselev, *Nanotechnology* **28**(6), 065704 (2017).
- ¹⁸N. Balke, S. Jesse, P. Yu, C. Ben, S. V. Kalinin, and A. Tselev, *Nanotechnology* **27**(42), 425707 (2016).
- ¹⁹L. Collins, Y. Liu, O. S. Ovchinnikova, and R. Proksch, *ACS Nano* **13**(7), 8055–8066 (2019).
- ²⁰A. Labuda and R. Proksch, *Appl. Phys. Lett.* **106**(25), 253103 (2015).
- ²¹L. Collins and U. Celano, *ACS Appl. Mater. Interfaces* **12**(37), 41659–41665 (2020).
- ²²S. S. Cheema, D. Kwon, N. Shanker, R. Dos Reis, S.-L. Hsu, J. Xiao, H. Zhang, R. Wagner, A. Datar, and M. R. McCarter, *Nature* **580**(7804), 478–482 (2020).
- ²³M. Nonnenmacher, M. o'Boyle, and H. K. Wickramasinghe, *Appl. Phys. Lett.* **58**(25), 2921–2923 (1991).
- ²⁴M. M. Shvabelman, A. G. Agronin, R. P. Urenski, Y. Rosenwaks, and G. I. Rosenman, *Nano Lett.* **2**(5), 455–458 (2002).
- ²⁵L. Collins, J. Kilpatrick, M. Bhaskaran, S. Sriram, S. A. Weber, S. Jarvis, and B. J. Rodriguez, in *Dual Harmonic Kelvin Probe Force Microscopy for Surface Potential Measurements of Ferroelectrics, Proceedings of ISAF-ECAPD-PFM 2012* (IEEE, 2012), pp. 1–4.
- ²⁶I. Gaponenko, L. Musy, N. Domingo, N. Stucki, A. Verdaguer, N. Bassiri-Gharb, and P. Paruch, *npj Comput. Mater.* **7**(1), 163 (2021).
- ²⁷E. Strelcov, A. V. Ievlev, S. Jesse, I. I. Kravchenko, V. Y. Shur, and S. V. Kalinin, *Adv. Mater.* **26**(6), 958–963 (2014).

- ²⁸F. a Saurenbach and B. Terris, *Appl. Phys. Lett.* **56**(17), 1703–1705 (1990).
- ²⁹E. Luo, Z. Xie, J. Xu, I. Wilson, and L. Zhao, *Phys. Rev. B* **61**(1), 203 (2000).
- ³⁰L. Fumagalli, D. Esteban-Ferrer, A. Cuervo, J. L. Carrascosa, and G. Gomila, *Nat. Mater.* **11**(9), 808–816 (2012).
- ³¹P. Ares, T. Cea, M. Holwill, Y. B. Wang, R. Roldan, F. Guinea, D. V. Andreeva, L. Fumagalli, K. S. Novoselov, and C. R. Woods, *Adv. Mater.* **32**(1), e1905504 (2020).
- ³²L. Fumagalli, A. Esfandiar, R. Fabregas, S. Hu, P. Ares, A. Janardanan, Q. Yang, B. Radha, T. Taniguchi, and K. Watanabe, *Science* **360**(6395), 1339–1342 (2018).
- ³³H. Balakrishnan, R. Millan-Solsona, M. Checa, R. Fabregas, L. Fumagalli, and G. Gomila, *Nanoscale* **13**(22), 10116–10126 (2021).
- ³⁴A. Kyndiah, M. Checa, F. Leonardi, R. Millan-Solsona, M. Di Muzio, S. Tanwar, L. Fumagalli, M. Mas-Torrent, and G. Gomila, *Adv. Funct. Mater.* **31**(5), 2008032 (2021).
- ³⁵M. Checa, R. Millan-Solsona, N. Blanco, E. Torrents, R. Fabregas, and G. Gomila, *Nanoscale* **11**(43), 20809–20819 (2019).
- ³⁶M. Checa, R. Millan-Solsona, A. G. Mares, S. Pujals, and G. Gomila, *Small Methods* **5**(7), 2100279 (2021).
- ³⁷M. Checa, R. Millan-Solsona, A. Glinkowska Mares, S. Pujals, and G. Gomila, *Nanomaterials* **11**(6), 1402 (2021).
- ³⁸G. Gomila, G. Gramse, and L. Fumagalli, *Nanotechnology* **25**(25), 255702 (2014).
- ³⁹L. M. Garten, D. T. Moore, S. U. Nanayakkara, S. Dwaraknath, P. Schulz, J. Wands, A. Rockett, B. Newell, K. A. Persson, and S. Trolier-McKinstry, *Sci. Adv.* **5**(1), eaas9311 (2019).
- ⁴⁰A. Tselev, P. Yu, Y. Cao, L. Dedon, L. Martin, S. Kalinin, and P. Maksymovych, *Nat. Commun.* **7**, 11630 (2016).
- ⁴¹Y. Cho, S. Kazuta, and K. Matsura, *Appl. Phys. Lett.* **75**(18), 2833–2835 (1999).
- ⁴²T. Sugihara and Y. Cho, *Nanotechnology* **17**(7), S162 (2006).
- ⁴³M. A. Susner, M. Chyasnavichyus, A. A. Puretzky, Q. He, B. S. Conner, Y. Ren, D. A. Cullen, P. Ganesh, D. Shin, and H. Demir, *ACS Nano* **11**(7), 7060–7073 (2017).
- ⁴⁴L. Fumagalli and G. Gomila, “Probing dielectric constant at the nanoscale with scanning probe microscopy,” in *Capacitance Spectroscopy of Semiconductors* (Pan Stanford Publishing, 2018).
- ⁴⁵L. Collins, M. Ahmadi, T. Wu, B. Hu, S. V. Kalinin, and S. Jesse, *ACS Nano* **11**(9), 8717–8729 (2017).
- ⁴⁶G. Gramse, G. Gomila, and L. Fumagalli, *Nanotechnology* **23**(20), 205703 (2012).
- ⁴⁷M. A. Susner, M. Chyasnavichyus, M. A. McGuire, P. Ganesh, and P. Maksymovych, *Adv. Mater.* **29**(38), 1602852 (2017).
- ⁴⁸S. Zhou, L. You, H. Zhou, Y. Pu, Z. Gui, and J. Wang, *Front. Phys.* **16**(1), 13301 (2021).
- ⁴⁹F. Liu, L. You, K. L. Seyler, X. Li, P. Yu, J. Lin, X. Wang, J. Zhou, H. Wang, H. He, S. T. Pantelides, W. Zhou, P. Sharma, X. Xu, P. M. Ajayan, J. Wang, and Z. Liu, *Nat. Commun.* **7**, 12357 (2016).
- ⁵⁰W. Huang, F. Wang, L. Yin, R. Cheng, Z. Wang, M. G. Sendeku, J. Wang, N. Li, Y. Yao, and J. He, *Adv. Mater.* **32**(14), e1908040 (2020).
- ⁵¹M. Si, P. Y. Liao, G. Qiu, Y. Duan, and P. D. Ye, *ACS Nano* **12**(7), 6700–6705 (2018).
- ⁵²J. A. Brehm, S. M. Neumayer, L. Tao, A. O’Hara, M. Chyasnavichus, M. A. Susner, M. A. McGuire, S. V. Kalinin, S. Jesse, P. Ganesh, S. T. Pantelides, P. Maksymovych, and N. Balke, *Nat. Mater.* **19**(1), 43–48 (2020).
- ⁵³K. S. Novoselov, A. K. Geim, S. V. Morozov, D-e Jiang, Y. Zhang, S. V. Dubonos, I. V. Grigorieva, and A. A. Firsov, *Science* **306**(5696), 666–669 (2004).
- ⁵⁴M. Chyasnavichyus, M. A. Susner, A. V. Ievlev, E. A. Eliseev, S. V. Kalinin, N. Balke, A. N. Morozovska, M. A. McGuire, and P. Maksymovych, *Appl. Phys. Lett.* **109**(17), 172901 (2016).
- ⁵⁵M. Van Der Hofstadt, R. Fabregas, M. C. Biagi, L. Fumagalli, and G. Gomila, *Nanotechnology* **27**(40), 405706 (2016).
- ⁵⁶D. Zhang, Z. D. Luo, Y. Yao, P. Schoenherr, C. Sha, Y. Pan, P. Sharma, M. Alexe, and J. Seidel, *Nano Lett.* **21**(2), 995–1002 (2021).
- ⁵⁷A. Belianinov, Q. He, A. Dziaugys, P. Maksymovych, E. Eliseev, A. Borisevich, A. Morozovska, J. Banys, Y. Vysochanskii, and S. V. Kalinin, *Nano Lett.* **15**(6), 3808–3814 (2015).
- ⁵⁸S. Jesse, A. Kumar, T. M. Arruda, Y. Kim, S. V. Kalinin, and F. Ciucci, *MRS Bull.* **37**(7), 651–658 (2012).
- ⁵⁹N. Balke, S. M. Neumayer, J. A. Brehm, M. A. Susner, B. J. Rodriguez, S. Jesse, S. V. Kalinin, S. T. Pantelides, M. A. McGuire, and P. Maksymovych, *ACS Appl Mater Interfaces* **10**(32), 27188–27194 (2018).
- ⁶⁰J. Banys, J. Macutkevic, V. Samulionis, A. Brilingas, and Y. Vysochanskii, *Phase Transitions* **77**(4), 345–358 (2004).